Enhancement of Conjugated Polymer Microstructure and Mixed-Conducting Properties via

Chalcogenophene Heteroatom Substitution

Bryan D. Paulsen, ^{1‡} Dilara Meli, ^{2‡} Maximilian Moser, ^{3‡} Adam Marks, ⁴ James F. Ponder Jr., ^{5†} Ruiheng Wu, ⁶ Emily A. Schafer, ¹ Joseph Strzalka, ⁷ Qingteng Zhang, ⁷ Iain McCulloch, ^{3*} Jonathan Rivnay ^{1,2,8*}

¹Department of Biomedical Engineering, Northwestern University, 2145 Sheridan Rd, Evanston, IL 60208, USA.

²Department of Materials Science and Engineering, Northwestern University, 2220 Campus Drive, Evanston, IL 60208, USA.

³Department of Chemistry, Chemistry Research Laboratory, University of Oxford, Oxford, OX1 3TA, UK.

⁴Department of Materials Science and Engineering, Stanford University, Stanford, CA 94305, USA

⁵Department of Chemistry and Centre for Plastic Electronics, Imperial College London, London, SW7 2AZ, UK.

⁶Department of Chemistry, Northwestern University, Evanston, Illinois 60208, USA.

⁷X-Ray Science Division, Argonne National Laboratory, Lemont, IL, 60439 USA.

⁸Simpson Querrey Institute, Northwestern University, Chicago, Illinois 60611, USA.

ABSTRACT

Heteroatom substitution is a powerful tool to tune the intra- and intermolecular structure of conjugated polymers, as well as their resulting optoelectronic and electrochemical properties. A series of oligoethylene glycol bithiophene chalcogenophene polymers (p(g3T2-X)) with systematically varied furan, thiophene, selenophene, and tellurophene comonomer have been synthesized for mixed ionic-electronic conducting applications. Their microstructure has been thoroughly characterized ex situ and in situ with X-ray scattering, and their mixed conducting properties have been probed in electrochemical transistor testbeds. Chalcogenophene heteroatom choice was found to clearly dictate polymer microstructure (crystallite dimensionality and orientation) and tune mixed conducting properties. Proceeding down Group 16, from O to Se systematically directed the molecular ordering of 2-D polymer crystallites from face-on (O) to mixed (S) to edge-on (Se) orientations, with Te driving the polymer to form well oriented edge-on 3-D crystallites. Heteroatom dictated crystallite quality and orientation tuned relative ionic transport by two orders of magnitude. Hole mobility (μ_{hole}) and mixed conducting figure of merit (μC^*) were each tuned over an order of magnitude depending on heteroatom choice, with the Te containing polymer reaching $\mu_{hole} = 3.60 \text{ cm}^2 \text{V}^{-1} \text{s}^{-1}$ and $\mu C^* = 483 \text{ Fcm}^{-1} \text{V}^{-1} \text{s}^{-1}$, due to improved molecular ordering. Insights from this polymer series highlight target microstructures for enhanced mixed conduction in future conjugated polymers.

INTRODUCTION

Organic mixed ionic-electronic conductors (OMIECs) bring together ionophilic functionality with extended π -conjugation to produce materials that efficiently transport and couple ionic and electronic charge.¹ As a burgeoning class of electroactive materials, OMIECs have wide applicability across energy storage,² actuator,³ electrochromic,⁴ light emitting,⁵ neuromorphic,^{6,7} bioelectronic,⁸ and catalytic applications.^{9,10} OMIECs are such an attractive materials class because of the opportunity to leverage their nearly infinite synthetic tunability to control the resulting material structure and properties. As an outgrowth of the larger field of organic electronics, OMIEC development has advanced rapidly by leveraging the many lessons learned in developing materials for organic field effect transistors, light emitting diodes, and photovoltaic devices. Considering just a subclass of OMIECs, conjugated polymers with oligoethylene glycol side chains, side-chain engineering (varying length, branching, regiochemistry, distribution, etc.) has become the most common route to control mixed conducting properties.^{11–13} With respect to the conjugated backbone, comonomer selection, ^{14–16} halogenation, ^{17,18} cyano functionalization, ¹⁹ and conformational locking.²⁰ have all been investigated.

Nearly universal to these materials is the incorporation of conjugated heterocycles, typically thiophene, into the polymer backbone. Despite the ubiquity of thiophene, relatively few studies of OMIECs incorporating other chalcogenophenes have been reported.^{21–24} Thiophene base chemistries are well established and incorporating other chalcogenophenes can present synthetic hurdles, especially for tellurophene (due to solubility and reactivity differences).²⁵ Nonetheless, substituting chalcogenophene heteroatoms are promising routes to tune frontier molecular orbital

levels, backbone planarity, and intermolecular interactions.²⁶ For these reasons, chalcogenophene heteroatom substitution applied to traditional organic field effect and photovoltaic devices has led to improved electronic charge transport and optical absorption, respectively.²⁷ Thus with OMIECs in mind, we have synthesized and investigated a series of alternating copolymers consisting of an oligoethylene glycol substituted bithiophene unit and an unsubstituted chalcogenophene unit (p(g3T2-X)), which has been systematically varied with furan (p(g3T2-O)), thiophene (p(g3T2-S)), selenophene (p(g3T2-Se)), and tellurophene (p(g3T2-Te)), as seen in Figure 1a. While our naming scheme emphasizes the substituted heteroatom, the all thiophene analogue (p(g3T2-S)) has elsewhere in the literature been referred to variously as g2T-T,²⁸ p(g2T-T),²⁹ and p(g3T2-T).¹² All polymers in the series showed ion uptake and transport, and p-type semiconducting behavior where electrochemical oxidation induced mobile hole carriers leading to efficient electronic charge transport.

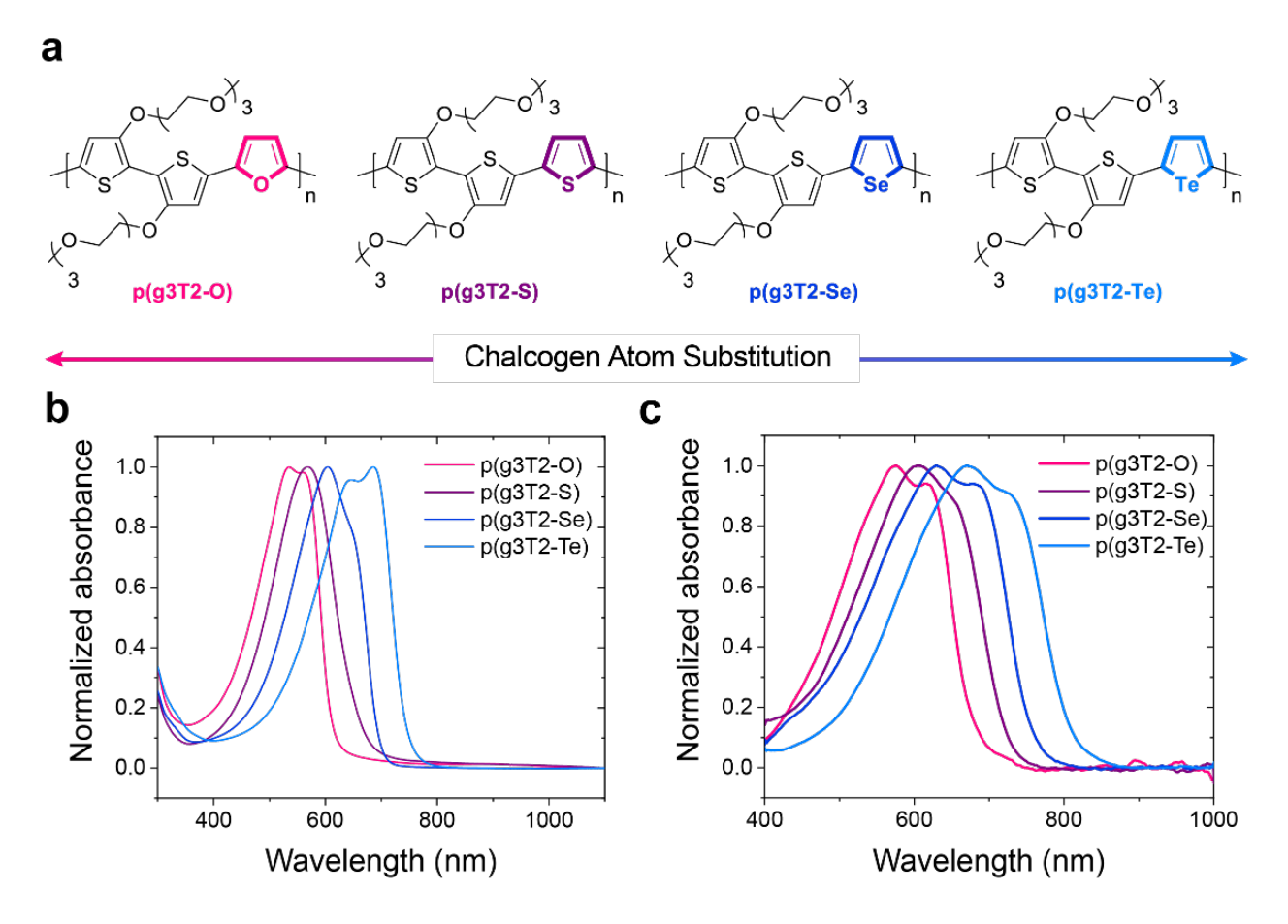


Figure 1. (a) Chemical structures, and (b) solution (CHCl₃) and (c) thin film UV-Vis absorption spectra of p(g3T2-O), p(g3T2-S), p(g3T2-Se), and p(g3T2-Te).

The optoelectronic properties of the polymer series were investigated with spectroscopic and electrochemical means, revealing LUMO stabilization and band-gap narrowing (Figure 1b&c). The microstructure of the polymer series was thoroughly characterized with ex situ and in situ grazing incidence X-ray scattering (GIWAXS), revealing the outsized influence that heteroatom choice plays in determining polymer ordering. Heteroatom choice was found to determine crystallite dimensionality and orientation, with the heaviest heteroatom investigated (Te) driving the formation of well oriented edge-on 3-D crystallites. Mixed conducting properties

were studied in organic electrochemical transistor (OECT) testbeds, where the doping state of p(g3T2-X) thin films in contact with aqueous electrolytes was controlled electrochemically, and the resulting electronic transport behavior was measured. Electronic transport was found to be highly correlated with polymer microstructure, with the best ordered p(g3T2-Te) showing an excellent OECT figure of merit, the product of the carrier mobility (μ_{hole}) and the volumetric capacitance (C^*), ($\mu_{hole} \times C^* = 483 \text{ Fcm}^{-1}\text{V}^{-1}\text{s}^{-1}$) with a low threshold voltage ($V_T = 0.04 \text{ V}$), and very sharp device turn on (S.S. = 44.3 ± 2.0 mV/decade), all a significant improvement over the more common all thiophene analogue. Further, ionic transport in p(g3T2-X) films in contact with aqueous electrolyte was probed across the polymer series and was found to be extremely sensitive to the heteroatom induced crystallite orientation. The heteroatom influence on stability was also investigated. Combined, our work establishes the utility of chalcogenophene heteroatom substitution as a route to control the structure and properties of OMIECs. Further, the systematic nature of this study revealed the structural features associated with enhanced electronic and ionic transport, which ought to be targeted by synthetic and/or processing means in future OMIEC materials research.

EXPERIMENTAL SECTION

Polymer synthesis. The polymer series was prepared via Stille polymerization using conventional conditions and purified by soxhlet extraction. Details on reagents, monomer synthesis, and polymerization conditions can be found in the Supporting Information.

Polymer characterization. UV-vis absorption spectra were measured under ambient conditions on a UV-1800 Shimadzu UV Spectrophotometer. Solution UV-vis absorption

spectroscopy was conducted on chloroform solutions with a polymer concentration of 0.008 mg mL-1. 1 H-NMR spectra were recorded on a Bruker AV-400 UltraShield spectrometer (400 MHz for 1 H) at 298 K and using chloroform-d (CDCl₃) as solvent, unless otherwise stated. Chemical shifts (δ) are expressed in parts per million (ppm) downfield from tetramethylsilane (TMS) and are referenced to chloroform ($\delta_{\rm H}$ 7.26 and $\delta_{\rm C}$ 77.16). Coupling constants (J) are expressed in Hertz (Hz) and multiplicities are indicated as singlet (s), doublet (d), triplet (t), quartet (q) or multiplet (m). Gel permeation chromatography (GPC) was measured using a PLgel 10 μ m Mixed-B column on an Agilent Technologies 1260 Infinity system with DMF as the mobile phase at 80 $^{\circ}$ C.

Electrochemistry. Cyclic voltammetry was performed employing an Autolab PGSTAT101 with a standard three-electrode configuration, including polymer coated ITO glass slides as the working electrode, a platinum wire as the counter electrode and a Ag/AgCl wire electrode as the reference electrode. The supporting electrolyte employed was either a 100 mM tetrabutylammonium hexafluorophosphate (TBAPF₆) in acetonitrile solution or a 100 mM sodium chloride (NaCl) in distilled water solution and scan speeds were 100 mV s⁻¹.

OECT test chips were prepared following microfabrication techniques previously reported.³⁰ OECT channels (L = 10 μm, W = 100 μm) were fabricated by spin-coating from chloroform (5 mg mL⁻¹, except pg3T2-Te which was 2.5 mg mL⁻¹) at 1500 rpm for 60 seconds onto OECT test chips at room temperature, followed by patterning via peeling a sacrificial parylene layer, and a rinse in deionized water. OECTs were gated with aqueous 100 mM NaCl using a Ag/AgCl pellet as the faradaic gate electrode (https://doi.org/10.1063/1.3491216). Electrical characterization (output, transfer curves, cycling stability, frequency dependent gain) of the OECTs were carried out using

an Ivium Technologies bipotentiostat. Capacitance was measured via electrochemical impedance spectroscopy (EIS) using the same potentiostat on 600 x 600 µm² planar gold electrodes.

Ex-situ grazing-incidence wide-angle X-ray scattering. 2-D GIWAXS sample films were spun from polymer solutions (5 mg mL⁻¹ in chloroform) on polished Si wafer substrates (University Wafer). Scattering was carried out at the Advanced Photon Source at Argonne National Laboratory on beam line 8- ID-E at room temperature under vacuum or He atmosphere with 10.92 keV (λ = 1.135 Å) synchrotron radiation, with a 0.14° incident angle, and measured with a Pilatus 1M hybrid pixel array detector during 30 second exposures. Data analysis was carried out with GIXSGUI Matlab toolbox³¹ and with custom curve fitting software. d-spacings were extracted from peak centers of pseudo-Voigt peak fits and coherence lengths were extracted from the fit FWHM.

In-situ grazing-incidence wide-angle X-ray scattering. In-situ GIWAXS samples were drop-casted onto glass slides coated with a sacrificial PVA layer. Films were float transferred in a water bath onto Au coated porous steel frits (Idex, 20 μm pore size).³² Scattering was carried out at the Stanford Synchrotron Radiation Lightsource at beamline 10-2. In-situ/operando scattering was carried out analogous to a previously reported setup, under hydrated He with 15.861 keV and 13.474 keV synchrotron radiation for pg3T2-Te and pg3T2-S, respectively, with a ~0.2° incident angle. An Ag/AgCl electrode was used as the reference electrode, bias was applied via a Ivium Technologies potentiostat.

RESULTS AND DISCUSSION

Polymer Synthesis and Characterization. Monomers were prepared as previously described in the literature, with additional details available in the Supporting Information. ^{13,24,33–35} Polymerization of p(g3T2-O) and p(g3T2-S) have been previously reported. ^{24,28} Polymerization of p(g3T2-Se) and p(g3T2-Te) of was achieved by employing analogous conditions as for p(g3T2-O) and p(g3T2-S), the details of which can be found in the Supporting Information.

 Table 1. Polymer Properties

Polymer	M_n (kg/mol)	Ð	λ _{max,soln} (nm)	$\lambda_{max,film}$ (nm)	$E_{gap,opt,sol}$ $^{n.}$ $(\mathrm{eV})^\mathrm{b}$	$E_{gap,opt,film} \ ({ m eV})^{ m c}$	Eox,org (V vs Ag/AgCl) ^d	Eox,qq (V vs Ag/AgCl) ^d
p(g3T2-O)	26.2	1.4	535	575	2.32	1.83	-0.03	-0.05
p(g3T2-S)	25.1	2.5	568	604	2.18	1.71	-0.12	-0.19
p(g3T2-Se)	15.3	1.6	604	630	2.05	1.64	-0.05	-0.13
p(g3T2-Te)	a	a	686	670	1.81	1.53	-0.12	-0.14

^aMolar mass of p(g3T2-Te) could not be determined accurately due to its insolubility in DMF and its insufficient refractive index contrast in an alternative eluent (CHCl₃) in which p(g3T2-Te) is soluble. ^bEstimated from the absorption onset of the solution phase UV-Vis. ^cEstimated from the absorption onset of the thin film UV-Vis. ^dEstimated from the onset of oxidation from cyclic voltammograms.

The polymer series was characterized by size exclusion chromatography, UV-Vis absorption spectroscopy, cyclic voltammetry, and spectroelectrochemistry, Table 1 and Figures 1b&c and S1-3. The increased heteroatom electronegativity descending group 16 correlated with decreased optical bandgap ($E_{gap,opt}$), in total narrowing 0.5 eV in solution and 0.3 eV in thin films from p(g3T2-O) to p(g3T2-Te). The electrochemical oxidation onsets (reflecting the HOMO level

position) did not follow a similar trend, and only varied 0.1 V vs Ag/AgCl (in organic electrolyte which gave the clearest oxidation onsets, Figures S2). This indicated that the primary effect of heteroatom substitution on electronic structure was LUMO stabilization, in keeping with previous studies.^{36,37} It is expected that the decreased aromaticity of furan, selenophene, and tellurophene with respect to thiophene would introduce more quinoidal nature, inducing more backbone planarity, and likely enhance intermolecular interactions (aggregation). ²⁶ This is evidenced in the solution absorption spectra (Figure 1b), where p(g3T2-O), p(g3T2-Se), and p(g3T2-Te) all show a vibronic shoulder/peak that is absent in the more aromatic p(g3T2-S), reflecting the formation of photophysical aggregates in solution (Figure 1b). Such preaggregation is likely more pronounced in p(g3T2-Te), which shows limited solubility (≤ 2.5 mg/ml in CHCl₃) and likely affects resultant thin film microstructure. However, in the solid state (thin film), p(g3T2-S) displays a vibronic shoulder, similar to the rest of the series (Figure 1c). Spectroelectrochemistry revealed similar behavior across the p(g3T2-X) series. Upon electrochemical oxidation the neutral π - π * absorption is successively quenched and higher wavelength (lower energy) absorption, indicative of (multi)polaronic species, 38,39 successively grows as charge density in the film increased with increased oxidative potential, Figure S3.

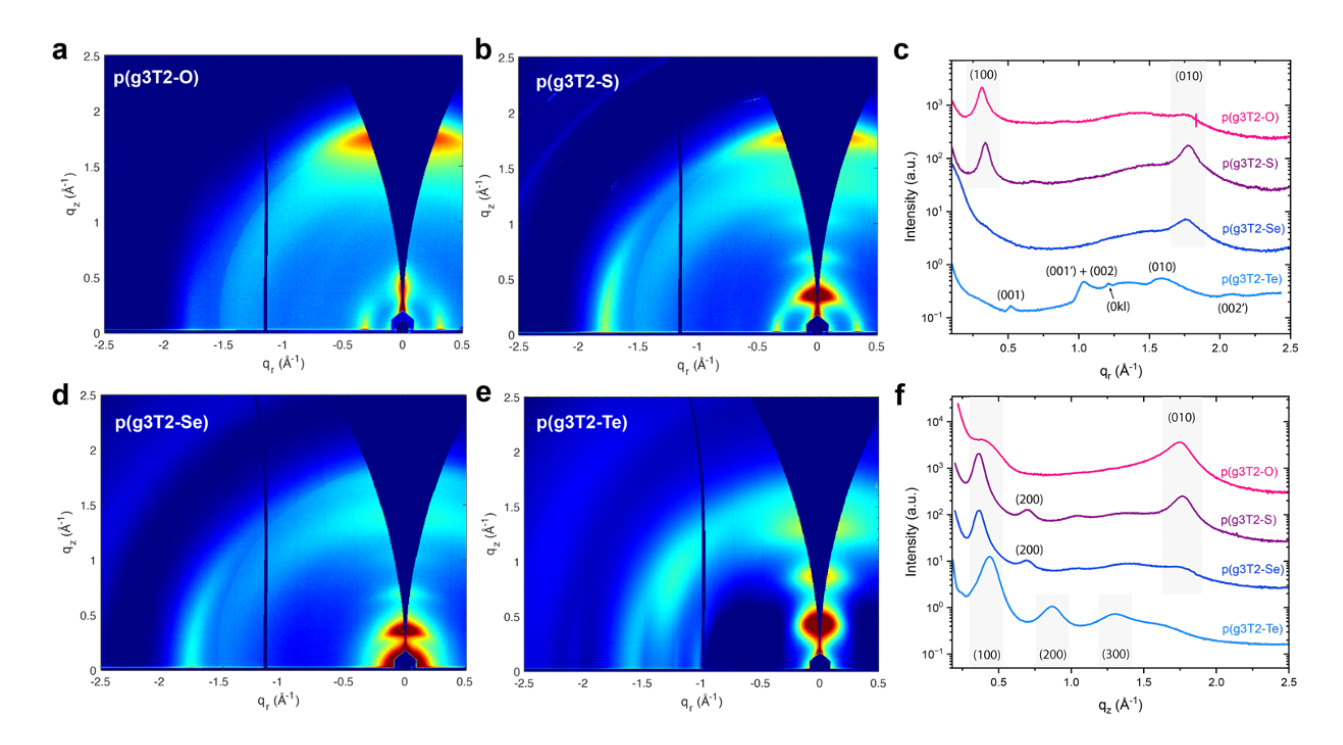


Figure 2. 2-D GIWAXS patterns (q_r - q_z maps of scattered X-ray intensity) of (a) p(g3T2-O), (b) p(g3T2-S), (d) p(g3T2-Se) and (e) p(g3T2-Te) spin coated thin films, as well as (c) in-plane (q_r) and (f) out-of-plane (q_z) line cuts of scattered X-ray intensity. Note the mixed-index scattering feature in panel (e) centered around $q_z \sim 0.95 \text{ Å}^{-1}$ and $q_r \sim 1.2 \text{ Å}^{-1}$.

Chalcogenophene Heteroatom Dependent Microstructure. Thin film microstructure across the series was probed with grazing incidence wide angle X-ray scattering (GIWAXS), as seen in Figure 2, revealing two general types of intermolecular ordering: one having moderately oriented 2-D crystallites with extensive ordering in the side-chain lamellar and π -stack directions; and a second having a well oriented 3-D crystallites with extensive ordering in the side-chain lamellar, π -stack, and polymer backbone directions.

p(g3T2-O), p(g3T2-S), and p(g3T2-Se) thin films all displayed a similar crystallite structure with characteristic lamellar (h00) and π -stack (0k0) scattering, Figure 2c & f. Across these three polymers, both lamellar and π -stack scattering manifest as relatively narrow arcs within the 2-D scattering patterns (Figure 2 a,b&e) indicating a rather narrow distribution of crystallite orientations.⁴⁰ Backbone peaks (001) were absent, suggesting that these three polymers lack significant periodic structure along the direction of the conjugated backbone. This is perhaps due to chain bending/twisting or the absence of any ordered co-facial registration between chains (i.e. π -stacked chains can slide along one another with no preference in registration between substituted bi-thiophenes and unsubstituted chalcogenophenes). Thus, the GIWAXS patterns indicate that ordered-domains (crystallites) are limited to two dimensions (π -stack and lamellar). These moderately textured 2-D crystallites, irrespective of face- or edge-on texture, are herein referred to simply as the 2-D crystallites, Figure 3c. Notably, in these 2-D crystallites the only direction along which electronic charge transport can occur that displays coherent ordering is the direction of the inter-chain π -stacking (as opposed to along the conjugated polymer backbone which is absent).

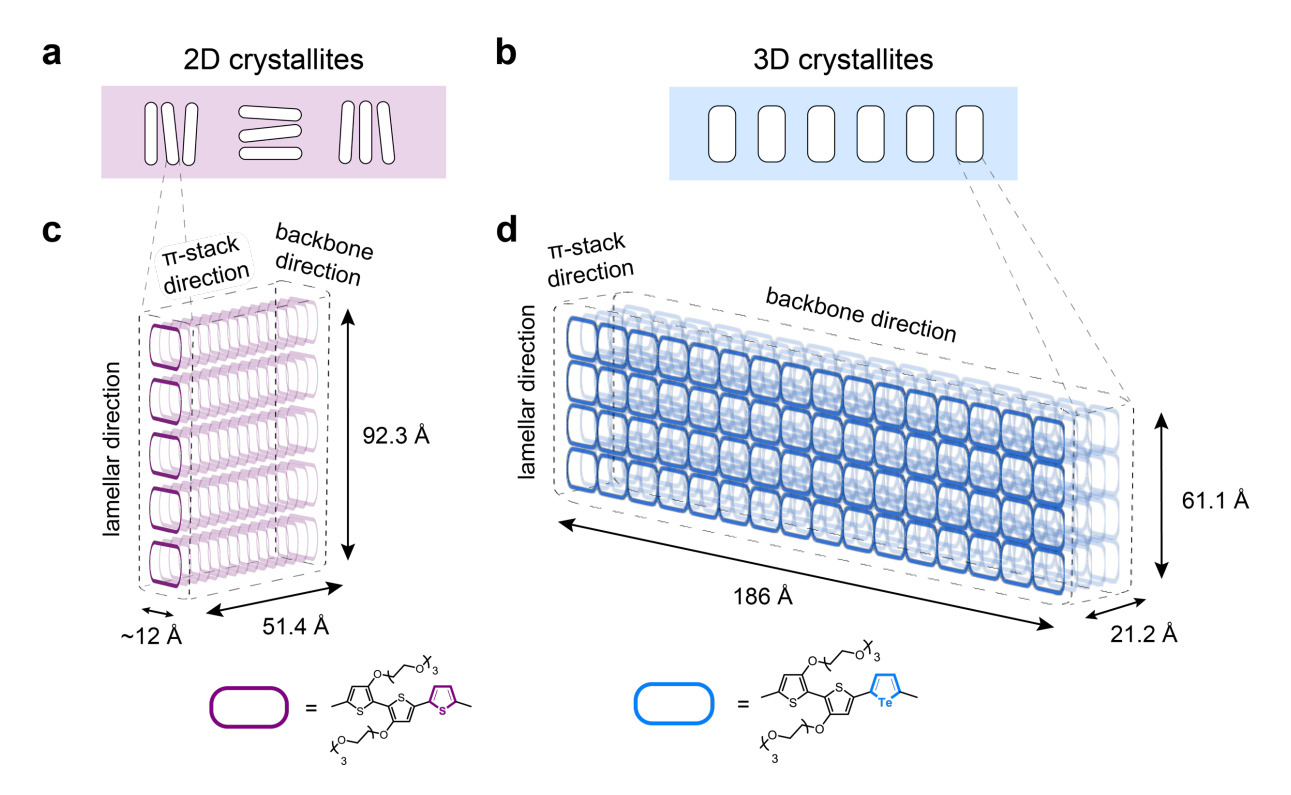


Figure 3. Illustrations of the orientation of (a) p(g3T2-S) and (b) p(g3T2-Te) crystallites within OECT channels (not drawn to scale), as well as dimensionality and coherence lengths of (c) the p(g3T2-S) 2-D crystallites and (d) the p(g3T2-Te) well oriented 3-D crystallites.

In p(g3T2-O), the predominantly in-plane lamellar and out-of-plane π -stack scattering (Figure 2a) indicates the 2-D crystallites largely have face-on orientation (with π -stacking perpendicular to the substrate), though with some distribution of orientation angles about perfectly face-on. Conversely in p(g3T2-Se), the predominantly in-plane π -stack and out-of-plane lamellar scattering (Figure 2d) indicates the 2-D crystallites largely have edge-on orientation (with lamellar-stacking perpendicular to the substrate), also with some distribution of orientation angles about perfectly edge-on. p(g3T2-S) presents an intermediate case showing distinct π -stack and lamellar scattering both in-plane and out-of-plane (Figure 2b), indicating a relative equal mix of

face- and edge-on 2-D crystallites, both with some distribution of orientation angles about perfectly edge- or face-on. Such chalcogenophene heteroatom directed crystallite orientation was not wholly unexpected as it has been observed before in other systems.^{41,42}

The p(g3T2-Te) GIWAXS presents a distinct case. The out-of-plane lamellar scattering is stronger than previous three polymers (with clear three orders of scattering peaks), and manifests not as arcs of scattered intensity, but instead as nearly perfectly round spots indicating well oriented crystallites with little variation about perfectly edge-on orientation, Figure 2e. 40 This is further bolstered by the presence of in-plane π -stack and backbone scattering features (Figure 2f) presenting as vertical rods with little radial or arc-like bend (Figure 2e). In-plane backbone scattering is consistent with a mix of two polymorphs with distinct co-facial registrations analogous to the behavior observed in N2200 (termed Form I or Form II polymorphs) and benzothiadiazole co-polymers (termed segregated or mixed polymorphs). 43-45 One co-facial registration is comprised of substituted bi-thiophene units aligned with adjacent substituted bithiophene units, and unsubstituted chalcogenophenes aligned with adjacent unsubstituted chalcogenophenes, leading to (001) peaks with a d-spacing (12.0 Å) which is comparable to the expected polymer repeat unit length (12.8 Å). The second co-facial registration is comprised of substituted bi-thiophene units aligned with adjacent unsubstituted chalcogenophene units and vice versa, leading to a halving of the unit cell, and (00l') peaks with a d-spacing (6.04 Å). The presence of Te appears to induce co-facial registration (both Form I and Form II). However, the stronger Te-Te interactions, arising from tellurium's metalloid character, 26 seem to increase the extent of ordering (as estimated by coherence length, Table S1) of Form I, where tellurophene is π -stacked with tellurophene.

While there are scattering peaks arising from ordering along the lamellar, π -stack, and backbone directions, the presence of mixed index scattering peaks (in- and out-of-plane) (Figure 2e,f) give strong evidence that these three dimensions of inter-chain ordering coexist in single 3-D crystallites.⁴⁶ These well oriented edge-on 3-D crystallites (Figure 3d) notably display coherent ordering in both directions of electronic transport (along the π -stacks and along the conjugated backbone), with the most extensive coherent ordering occurring along the direction of the polymer's conjugated backbone. While previous work has shown that tellurophene incorporation increased the intensity of X-ray scattering (i.e. more crystallites) of donor-acceptor copolymers,³⁷ this heteroatom dependent transition from a 2-D to 3-D crystallites has apparently not been observed before.

Intermolecular d-spacings and coherence lengths of inter-molecular ordering in each direction were calculated from peak fits from in- and out-of-plane line cuts (Table S1).⁴⁰ In the 2-D crystallites, lamellar d-spacings were ~17 Å out-of-plane and 18-20 Å in-plane. Lamellar coherence lengths were similar, ranging from 90 to 105 Å, reflecting six to seven chains separated by their oligo ethylene glycol sidechains layered coherently as to give rise to X-ray scattering. The d-spacings in the π -stack were similar (between 3.5 and 3.6 Å) across the three polymers displaying 2-D crystallites. However, π -stack coherence lengths varied across polymer and orientation, being lowest in p(g3T2-Se) at 30 Å (~10 in-plane π -stacked chains), followed by 41 Å (~12 out-of-plane π -stacked chains) in p(g3T2-O). These were exceeded by both the in- and out-of-plane π -stack coherences lengths in p(g3T2-S) at 51 Å (~15 in-plane π -stacked chains) and 43 Å (~13 out-of-plane π -stacked chains), respectively.

The well oriented 3-D crystallites that manifest in p(g3T2-Te), showed a tighter lamellar d-spacing (14.4 Å), but an expanded π -stack d-spacing (3.91Å), in comparison with the less

oriented 2-D crystallites. Additionally, compared to the 2-D crystallites, the lamellar and π -stack coherence lengths were somewhat diminished, being 61 Å (~5 lamellar stacked chains) and 21 Å (~6 π -stacked chains), respectively. However, whereas the 2-D crystallites exhibited no backbone scattering (and thus no coherence lengths), the p(g3T2-Te) (001) backbone coherence length was 186 Å, reflecting a coherent ordering spanning ~45 heterocyclic rings down the polymer backbone.

Summarizing these structural findings, when varying the unsubstituted chalcogenophene heteroatom; p(g3T2-O), p(g3T2-S), and p(g3T2-Se) present similar 2-D crystallites where the π -stacking direction is the only direction of coherent molecular ordering present in which electronic transport is expected to occur. Descending down group 16 (O, S, Se), the orientation is tuned from face-on (O), to a mix of face- and edge-on (S), to edge-on (Se), where the mixed orientation p(g3T2-S) displays the largest extents of π -stack coherence. Descending further down group 16 to Te, the p(g3T2-Te) manifests distinct well edge-on oriented 3-D crystallites, of markedly improved crystallite quality, where coherent molecular ordering is present in both the π -stacking and backbone directions, and along the backbone is the charge transport direction with the most extensive ordering. These structural trends are correlated with mixed ionic-electronic conducting transport behavior below, but two further approaches were taken to better understand the origins and persistence of these 2-D and 3-D crystallites.

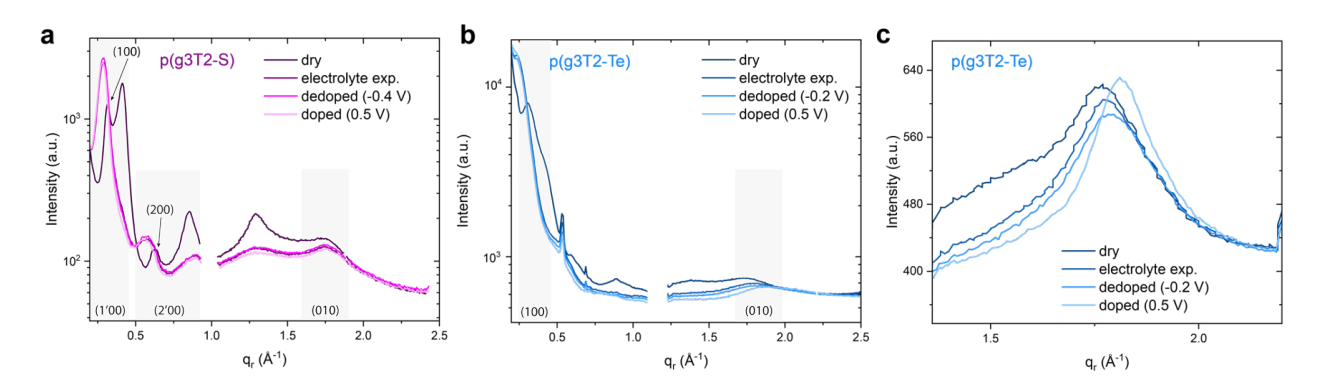


Figure 4. Out-of-plane (q_z) line cuts of scattered X-ray intensity of dropcast films of (a) p(g3T2-S) and (b) p(g3T2-Te) films, as well as (c) in-plane (q_r) line cuts highlighting π -stacking of p(g3T2-Te) films, in the dry as-cast state, and in situ during electrolyte exposure, electrochemical dedoping (reduction to neutral), and electrochemical doping (oxidation).

In Situ Microstructure. First, a comparison of GIWAXS of drop-cast films of p(g3T2-S) and p(g3T2-Te) was carried out, Figure 4. It is theorized that the slower solvent evaporation (in comparison to spin-coating) might allow for improved ordering. ⁴⁶ In the case of drop-cast p(g3T2-S), the original spin-coated 2-D crystallites were present (with a d-spacing of 20.1 Å) in an addition to a second polymorph with narrower lamellar d-spacings (15.2 Å), Figure 4a. However, no backbone or mixed index scattering was apparent, and the arc-like shape of the scattering indicated significant distribution of crystallite orientations, Figure S4a. The drop-cast p(g3T2-Te) displayed a complex mix of lamellar scattering features reflecting two polymorphs with distinct d-spacings: a stronger set of peaks (three orders) with a d-spacing of 20 Å and a weaker set of shoulders (two orders) with a d-spacing of ~27 Å, Figure 4b. Both of these d-spacings were considerably larger than that of spin-coated p(g3T2-Te), due either to side chain extension, or in the case of the largest

lamellar d-spacings a possible unit cell doubling in the direction of the lamellar stacking. While the lamellar d-spacings were expanded with respect to the spin-coated films, the π -stack d-spacing was significantly tightened (3.53 Å), Figure 4c. Despite these d-spacing differences, the drop-cast films' lamellar scattering in the p(g3T2-Te) maintained a round spot shape, indicating well oriented crystallites, Figure S4e. Further, backbone and mixed-index peaks were present indicating 3-D crystallites, in keeping with the spin-coated structure.

These drop-cast films were amenable to in situ scattering during electrolyte exposure and electrochemical cycling using a frit-based cell previously reported.³² Upon electrolyte exposure both films underwent a transformation to a single crystallite structure, Figure 4a&b. In the case of p(g3T2-S), the scattering from crystallites with tighter lamellar spacing disappeared, and a single population of crystallites with a lamellar d-spacing of 21.8 Å persisted. In p(g3T2-Te), a single population of crystallites with a lamellar d-spacing of 26.1 Å persisted. Electrochemical cycling between doped (oxidized) and de-doped (reduced to neutral) states modestly modulated the lamellar spacings of both films (0.3 Å), Figure 4a&b. The p(g3T2-S) π -stack d-spacing was unaffected by electrolyte exposure and electrochemical cycling, the p(g3T2-Te) π -stack (010) scattering was systematically influenced, having enhanced scattering and tightest d-spacing in the doped (oxidized) state, Figure 4c. Importantly, even after electrolyte exposure and electrochemical cycling p(g3T2-Te) lamellar scattering maintained a round spot shape (Figure Sf-h), reflecting the presence of well oriented edge-on crystallites, indicating that the distinct crystallite differences observed ex situ persist in actual device operating conditions. In summary, though drop-casting could introduce distinct populations of polymorphs, these coexisting polymorphs were insufficiently stable, and disappeared upon electrolyte exposure, leaving only the original (similar

to spin-coated) 2-D crystallites or well oriented 3-D crystallites that were stable during electrolyte exposure and electrochemical cycling.

Side-Chain Length Dependent Microstructure. The final approach sought to better understand the balance of side-chain and π -stack interactions in dictating crystallite structure by comparing the series at hand with analogous polymers with oligoethylene glycol side chains extended by one glycol repeat unit. Thus p(g4T2-O), p(g4T2-Se), and p(g4T2-Te) where synthesized and investigated with ex situ GIWAXS, Figure 5. Scattering peaks were fit to extract both d-spacings and coherence lengths, Table S2. p(g4T2-S) has been previously synthesized, investigated with GIWAXS, and reported elsewhere. It was theorized that longer side chains would strengthen the effect of side chain ordering (which is less sensitive to chalcogenophene heteroatom) in determining ultimate crystallite ordering, perhaps over and against π -stack ordering (which is more sensitive to chalcogenophene heteroatom).

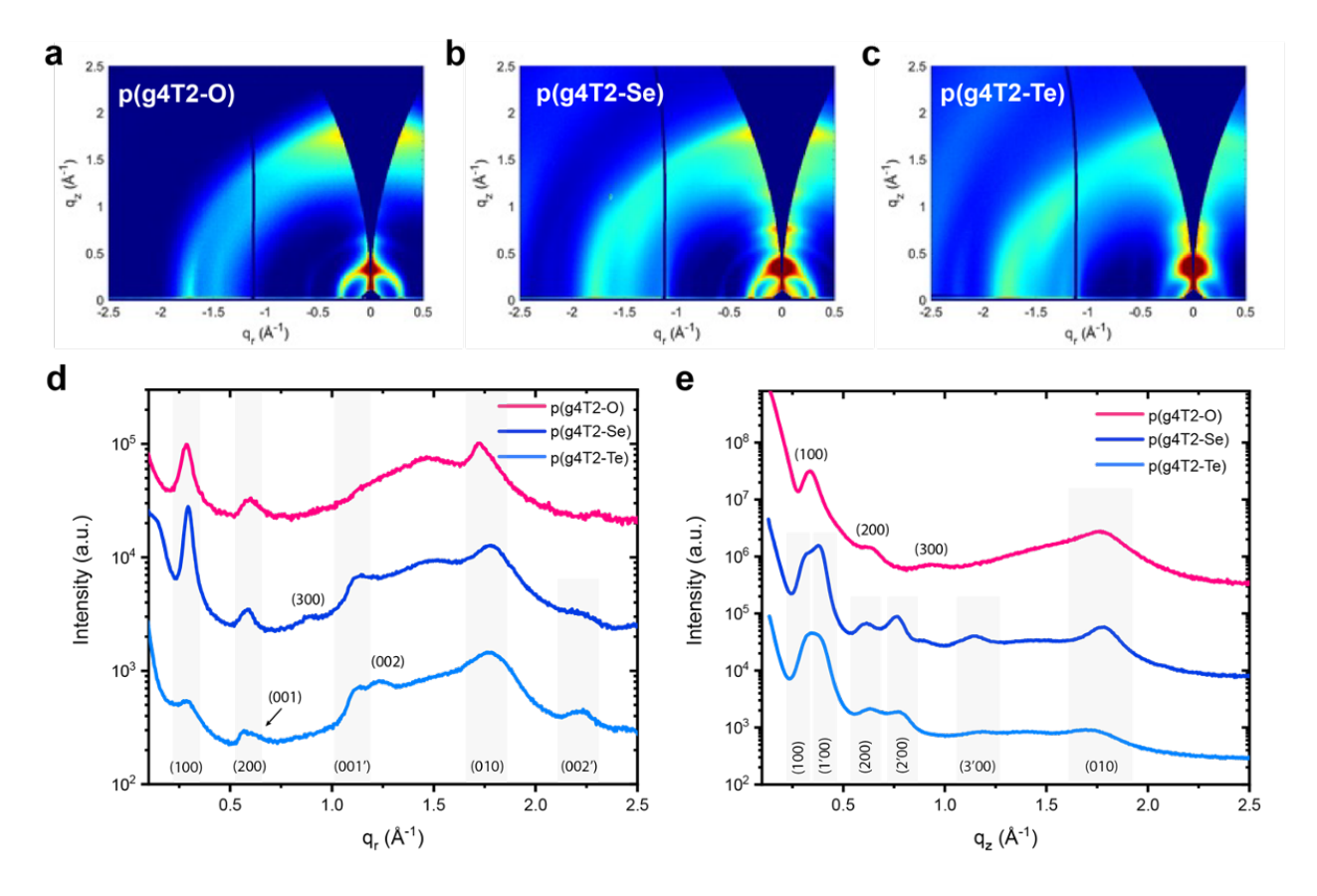


Figure 5. 2-D GIWAXS patterns (q_r - q_z maps of scattered X-ray intensity) of (a) p(g4T2-O), (b) p(g4T2-Se), and (c) p(g4T2-Te) spin coated thin films, as well as (d) in-plane (q_r) and (e) out-of-plane (q_z) line cuts of scattered X-ray intensity.

In the case of p(g4T2-O), the lengthened g4 side chain did seem to diminish the effect of the furan that drove p(g3T2-O) to adopt a majority face-on orientation. Instead, the p(g4T2-O) showed a mix of edge- and face-on crystallite orientations (Figure 5a), very similar to the p(g3T2-S) microstructure (Figure 2b), and consistent with the 2-D crystallites. Line cut analysis revealed that the d-spacings and coherence lengths were in keeping with the above 3g 2-D crystallites, with an increased lamellar spacing reflecting a longer oligoethylene glycol side chain. Thus, for 2-D

crystallite p(gXT2-O) polymers, longer side chains attenuated the heteroatom effect on crystallite orientation.

In the case of p(g4T2-Se), the lengthened g4 side chain gave rise to the coexistence of polymorphs of both moderately edge- and face-on oriented 2-D crystallites, with well edge-on oriented 3-D crystallites, Figure 5b. This was evidenced by the presence of in- and out-of-plane lamellar scattering arcs (consistent with the 2-D crystallites in face- and edge-on orientations) (Figure 5b,d&e); as well as strong round out-of-plane lamellar spots, out-of-plane mixed index scattering, (Figure 5b) and in-plane backbone scattering (Figure 5e) (all consistent with the well oriented edge-on 3-D crystallites). This coexistence of the two polymorphs is most clearly seen in the out-of-plane line cuts, Figure 5e. Thus, similar to the case of p(g4T2-O), extending the side-chain length in p(g4T2-Se) attenuates the heteroatom preference for a particular crystallite orientation (edge-on), but also attenuates the heteroatom preference for the 2-D crystallites, allowing the formation of the 3-D well oriented edge-on crystallites.

Extending the side-chain length in p(g4T2-Te) attenuates the heteroatom preference for the well oriented edge-on 3-D crystallites, allowing the formation of 2-D crystallites with a majority edge-on orientation, Figure 5c. This is evidenced by the presence of strong round out-of-plane lamellar spots, out-of-plane mixed index scattering, (Figure 5c) and in-plane backbone scattering (Figure 5e) (all consistent with the well oriented edge-on 3-D crystallites); as well as out-of-plane lamellar scattering arcs (consistent with the 2-D crystallites), though with a narrower radial spread than p(g4T2-Se), indicating a narrower distribution of edge-on 2-D crystallites. Again, this coexistence of polymorphs is most clearly seen in the in-plane line cuts, Figure 5e. Line cut analysis of p(g4T2-Se) and p(g4T2-Te) revealed that the d-spacings and coherence lengths were roughly in keeping with the respective 3g polymers, with an increased lamellar spacing reflecting

a longer oligoethylene glycol side chain, and decreased backbone coherence compared to the 3g polymers. Considering both the 3g and 4g heteroatom series, it became apparent that through selection of side-chain length and chalcogenophene heteroatom, the selection of moderately oriented 2-D or well oriented edge-on 3-D crystallites, the selection in- or out-of-plane crystallite orientation, and combinations there-in, can be rationally targeted.

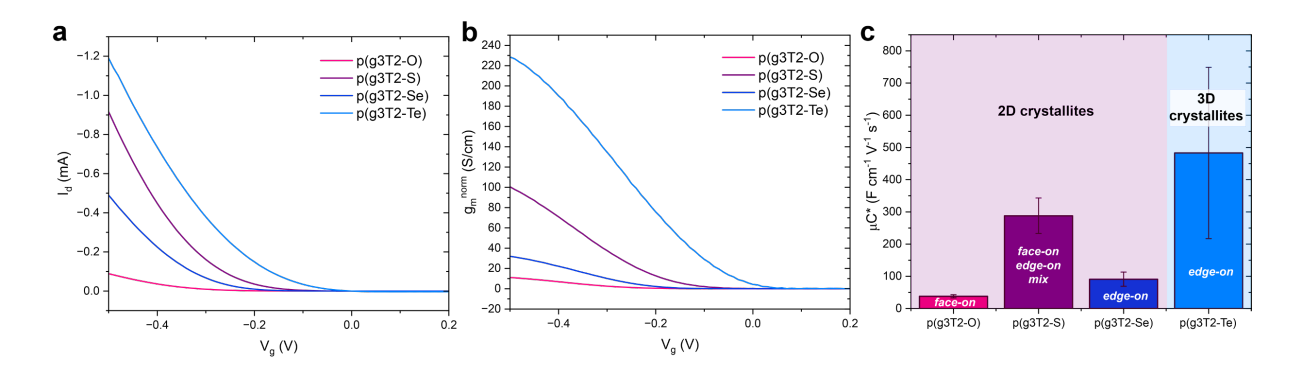


Figure 6. Representative (a) transfer curves, (b) gate voltage dependent transconductance, and (c) average μ C* of OECTs with p(g3T2-O), p(g3T2-Se), p(g3T2-Se), and p(g3T2-Te) channels operated in the saturation regime.

Electronic Transport. In order to investigate the effect of chalcogenophene heteroatom choice on electronic transport, OECTs were fabricated incorporating spin-coated transistor channels of p(g3T2-O), p(g3T2-S), p(g3T2-Se), and p(g3T2-Te). All materials other than p(g3T2-O), which drops out of saturation beyond -0.6 V, showed clear transistor behavior with output characteristics showing drain voltage dependent saturation, Figure S5. Transfer curves were collected in order to extract threshold voltage (V_T), subthreshold slope (S.S.), and gate

transconductance (g_m) (Figure 6a&b and S7a). Saturated hole mobility (μ_{hole}) and OECT figure of merit μC^* , the product of carrier mobility and volumetric capacitance (C^*) , were calculated from g_m , following equation (1) for accumulation mode devices,

$$g_m = \frac{Wd}{L} \mu C^* (V_G - V_T) (1)$$

where channel width (W) and length (L) were determined by the lithographically patterned source and drain electrodes, channel depth (d) was measured by profilometry, V_G was the applied gate voltage (Figure 6c).

Table 2. OECT parameters and material figures of merit.

Polymer	HOMOaq,est	- <i>V</i> _T (V) ^b	S.S. (mV/dec.)	gm,max,norm. (S cm ⁻¹) ^c	C* (Fcm ⁻ ³) ^d	$(\text{cm}^2\text{V}^{-1}\text{s}^{-1})^{\text{e}}$	$\mu_{hole} x C^*$ (Fcm ⁻¹ V ⁻¹ s ⁻¹)	$\mu C^*_{@gm,max}$ $(\text{Fcm}^{-1}\text{V}^{-1}\text{s}^{-1})^{\text{f}}$
p(g3T2-O)	4.58	0.218 ± 0.002	106.8 ± 2.4	14 ± 5	170 ± 15	0.21 ± 0.03	38 ± 5	29 ± 5
p(g3T2-S)	4.44	0.155 ± 0.003	72.9 ± 3.3	122 ± 43	208 ± 30	1.38 ± 0.17	288 ± 55	223 ± 56
p(g3T2-Se)	4.50	0.178 ± 0.008	~95 ^g	33 ± 17	99 ± 5	0.92 ± 0.22	91 ± 22	64 ± 18
p(g3T2-Te)	4.49	0.037 ± 0.003	44.3 ± 2.0	214 ± 159	134 ±15	3.60 ± 1.92	483 ± 266	462 ± 264

^aEstimated from the oxidation onset in aqueous media assuming the $E_{Ag/AgCl} = 4.626$ eV below vacuum level. ^bExtracted from the zero current intercept of the linear region of $I_d^{1/2}$ vs V_g plots (Figure S7c) in OECTs with a Ag/AgCl pellet functioning as the faradaic gate electrode. ^cMaximum slope of the saturated transfer curve normalized by device dimensions (Wd/L). ^dAverage volumetric capacitance beyond threshold voltage determined by electrochemical impedance spectroscopy. ^cCalculated from the slope of $I_d^{1/2}$ vs V_g plots (Figure S7c). ^fCalculated from the maximum transconductance (Figure S7b). ^gHigh off currents inhibited an accurate *S.S.*

determination of p(g3T2-Se), with the minimum S.S. reaching \sim 95 mV/decade. Reported uncertainties are one standard deviation, with n = 6 devices.

 C^* was assessed via electrochemical impedance spectroscopy, Figure S6. While there was some variation in C^* , the μ_{hole} variation was larger such that the μC^* closely tracked μ_{hole} . Overall, OECT performance (Table 2) did not follow the optoelectronic trends (reflecting intramolecular structure. Table 1), but instead followed the structural trends (reflecting intermolecular structure). While these materials assuredly have large amorphous fractions, OMIEC electronic transport is often highly correlated with crystalline microstructure, 47,48 and here the comparison of the crystallite microstructure and electronic charge transport reveals instructive correlations. μ_{hole} and μC^* were highest in p(g3T2-Te) with the well oriented 3-D crystallites which had the best quality of crystallite ordering. Amongst the polymers displaying the 2-D crystallites, μ_{hole} and μC^* was maximized in the mixed face- and edge-on p(g3T2-S), with the majority face-on p(g3T2-O) and majority edge-on p(g3T2-Se) both showing poorer electronic transport. The structural rationale followed that a three dimensionally ordered polymer, such as p(g3T2-Te), with extensive ordering in both the backbone and π -stack directions (along which electronic charge can transport) would be expected to have better charge transport than a similar two dimensionally ordered polymers. In fact, the p(g3T2-Te) μ_{hole} (3.60 ± 1.92 cm²V⁻¹s⁻¹) and μC^* (483 ± 266 Fcm⁻¹V⁻¹s⁻¹) place it amongst the top performing polymeric p-type accumulation mode OECT channel materials.⁴⁹

Since OECTs undergo volumetric doping and three-dimensional electronic charge transport, polymers that exhibit ordering along the π -stack direction (but not along the backbone direction) might be presumed to have the best electronic charge transport in films with π -stack

crystallites showing both in- and out-of-plane orientations, followed by films with only in-plane π -stacking (which is consonant with macroscopic in-plane transport between the source and drain electrodes), and finally the worst charge transport would be expected in films with only out-of-plane π -stacking (which is orthogonal to the macroscopic in-plane charge transport between the source and drain electrode). In fact, this is exactly the structure-transport relationship observed amongst the polymers exhibiting the 2-D crystallites, with μ_{hole} and μC^* following the trend p(g3T2-S) > p(g3T2-Se) > p(g3T2-O). The three-dimensional nature of charge transport in OECTs makes them distinct from two dimensional devices, such as organic field effect transistors, in which chalcogenophene homopolymers show a steady order-of-magnitude field effect mobility enhancement as the heteroatom is substituted from sulfur, to selenium, to tellurium.⁵⁰

Considering the OECT turn-on behavior, V_T lagged considerably behind $E_{OX,aq}$, by 0.18 V p(g3T2-Te) up to 0.35 V for p(g3T2-S), indicating that significant charge accumulation precedes appreciable channel conductance. Further, as the electrochemical potentials are directly relatable to frontier molecular orbital energy levels, it was found that V_T was not correlated with the polymer HOMO levels, Table 2. Instead, device V_T depended strongly on subthreshold behavior (i.e. how strongly the device turns on from the insulating state). Subthreshold slope (S.S.), measured in mV of gate voltage per decade increase in drain current, was extracted from semi-log transfer curves (Figure S8). S.S. followed the overall structure-transport trends with p(g3T2-Te) < p(g3T2-S) < p(g3T2-Se) < p(g3T2-O) (a low S.S. indicates a better performing device). The low S.S. of p(g3T2-Te) (44.3 \pm 2.0 mV/decade) was ascribed to the well-ordered microstructure of its well oriented 3-D crystallites, as improved ordering likely decreases trap density and narrows the electronic density of states. S1-53 Such a low S.S. should not be interpreted as breaking the room temperature thermodynamic limit of S.S. found in field effect devices (60 mV/decade at 300K). OECTs are not

field effect devices and do not necessarily follow the same fundamental device physics. In OECTs, charge density can be modulated by up to 10²¹ holes cm⁻³ through electrochemical doping.⁵⁴ Concomitantly, carrier mobility (which may actually decrease upon initial doping)⁵⁵ can span four orders of magnitude, resulting in over seven orders of magnitude of channel conductance modulation over less than a single volt of applied electrochemical potential.^{56–58} This is compounded by the use of faradaic gate electrodes (such as Ag/AgCl employed here), where the stable electrode potential minimizes potential drop at the gate-electrolyte interface,⁵⁹ further minimizing the applied gate potential required to modulate electrochemical doping and electronic conductivity. Thus, it is conceivable that OECT *S.S.* reach values less than 60 mV/decade, and in fact previous studies have shown electrochemically modulated conductivities with variations below 50 mV/decade.⁵⁵ Such potentially steep subthreshold behavior makes already low voltage OECTs even more attractive for low power electronics.

Summarizing the electronic transport results, well oriented 3-D crystallites present in p(g3T2-Te) correlated with improved OECT behavior according to all metrics (μ_{hole} , μC^* , V_T , S.S.), revealing the relative benefits of a well ordered OMIEC. Otherwise, in less ideal 2-D ordered polymers, a mix of edge- and face-on oriented crystallites is required to maximize electronic transport.

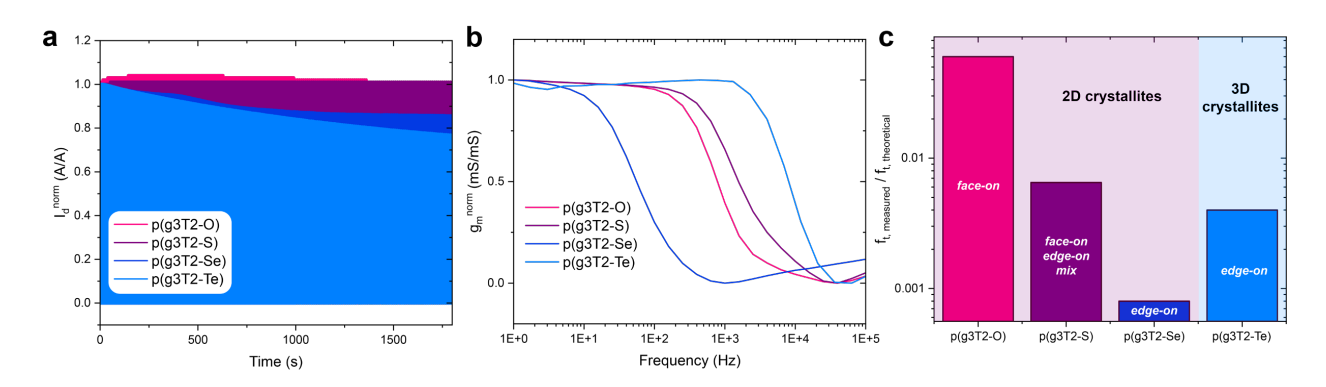


Figure 7. OECT (a) drain current stability during cycling V_G from 0 to -0.5 V in saturation, (b) frequency dependent gate transconductance with a 10 mV AC oscillation and a V_G offset of -0.5 V, (c) and ratio of actual OECT roll-off frequency and theoretical cut-off frequency indicating the degree to which ionic transport limits OECT operation.

Electrochemical Stability. Chalcogenophene heteroatom substitution was expected to affect chemical reactivity and thus OECT device stability, with furan and tellurophene expected to be particularly susceptible to degradation. Successive of OECT stability are increased in bioelectronic applications where aqueous electrolytes including dissolved oxygen are used, and ambient air and light may be present. To assess polymer stability in OECT applications, devices were repetitively cycled in saturation while the drain currents were monitored, Figure 7a. After 450 cycles out to a V_G of -0.5 V, p(g3T2-O) and p(g3T2-S) OECTs showed no degradation in maximum drain current, with V_T and gate voltage dependent g_m being identical before and after cycling, Figure S9a&b. While cycling, p(g3T2-Se) OECT maximum drain current appeared to initially drop and then stabilize (plateau) at 87% of the initial maximum drain current, while p(g3T2-Te) maximum drain current dropped to 78% of the initial value without stabilizing, with

both showing a decrease in the gate voltage dependent g_m while V_T remained unchanged, Figure S9c.

OECTs were then subjected to a successive round of 450 cycles, but now out to a larger V_G of -0.7 V, still in saturation, Figure S9e-h. Again, p(g3T2-S) OECTs showed no degradation in maximum drain current, with V_T and gate voltage dependent g_m being identical before and after cycling, Figure S9f. The previous stabilization of p(g3T2-Se) when cycled to a V_G of -0.5 V persisted when further cycled to a V_G of -0.7 V, as the maximum drain current was nearly constant, Figure S9g. However, this masked a subtle decrease in both voltage dependent g_m and V_T which counteracted each other such that peak drain current dropped only slightly (<5%). With further cycling to a V_G of -0.7 V, p(g3T2-O) maximum drain current dropped an additional 35% without stabilizing, showing a further decrease in the gate voltage dependent g_m while V_T remained unchanged, Figure S9e. p(g3T2-Te) OECTs where quite unstable under these conditions, with drain currents rapidly degraded after just a few cycles to a V_G of -0.7 V.

Overall, OECTs followed the stability trend of p(g3T2-S) > p(g3T2-Se) > p(g3T2-O) > p(g3T2-Te). Interestingly, electrochemical cycling of p(g3T2-Te) with in situ GIWAXS under inert and ambient conditions revealed no structural degradation to accompany electronic transport degradation, indicating that the loss of electrical conductivity arose from sources other than a large scale microstructural disruption. These OECT stability issues are not insurmountable as previous studies have shown that electrode modification, alternative biasing schemes, and electrolyte interlayer can slow OECT degradation, even in furan containing polymers.^{24,61}

Ionic Transport. In order to assess the ease of ion transport in these mixed conducting polymers, frequency dependent OECT measurements of OECT g_m were carried out to assess the

degree to which ionic transport limits OECT functioning, Figures 7b&c and S10. Given that OECTs incorporating mixed conducting channel materials, the frequency dependent OECT behavior is dependent on device geometry, electronic transport, and ionic transport. If electronic transport alone is the rate limiting transport, then the OECT cut-off frequency (f_T), where the current gain drops to unity, can be calculated from equation (2) below,

$$f_T = \frac{\mu_{hole} | (V_G - V_T) |}{2L^2} (2)$$

where L is the OECT channel length. For an explanation of the derivation and device geometry considerations see the Supporting Information. Because of difficulties accurately measuring where the current gain reaches unity, the readily assessed roll-off frequency f_R where gm falls below 90% of its low frequency value was instead extracted (assuming a RC-like 20 dB/decade roll off, f_R should be $\sim 0.5 \, f_T$). However, none of the materials produced OECTs where the measured roll-off frequency approached the theoretical electronic limited cut-off frequency. Instead, it became apparent that ionic transport limited the upper limit of device operating frequency.

To quantify the degree to which ionic transport limited OECT high frequency behavior, the measured f_R was divided by the theoretical f_T , Figure 7c. p(g3T2-O) most closely approached the theoretical limit ($f_R / f_T = 0.06$), however p(g3T2-S) was an order of magnitude lower ($f_R / f_T = 6.5 \times 10^{-3}$), and p(g3T2-Se) was a further order of magnitude lower ($f_R / f_T = 8 \times 10^{-4}$), indicating ionic transport was drastically slowed with heavier and heavier chalcogenophene heteroatom. It is not expected that direct ion-heteroatom interactions would give rise to such a drastic tuning of ionic transport, and previous studies have reported minimal dependence of ionic transport on chalcogenophene heteroatom.²¹ Thus, it is presumed that these large differences in ionic transport have a microstructural origin.

Considering the geometry of OECTs, the primary ionic transport direction was perpendicular into the OMIEC channel, through thin film thickness. In p(g3T2-O) based OECTs, crystallites are majority face-on oriented with π -stacks perpendicular to the substrate, thus the ionophilic oligoethylene glycol side chain lamellae are oriented such that they present as nanoscopic ionophilic channels oriented into the film thickness through which ions may preferentially travel, Figure S10e. Conversely, in p(g3T2-Se) based OECTs, crystallites are majority edge-on oriented with π -stacks parallel to the substrate. This presents alternating layers of ionophobic π -stacking and ionophilic oligoethylene glycol side chain lamellae that must be traversed by ions transporting through film thickness, Figure S10f. This in part may explain why ion transport in p(g3T2-Se) is suppressed by two orders of magnitude with respect to the rather facile ion transport in p(g3T2-O).

p(g3T2-S), containing a mix of face- and edge-on crystallites presents a middle case of some face-on ordering that is potentially advantageous to ionic transport (and some is edge-on ordering that is potentially disadvantageous to ionic transport), which is reflected in f_R/f_T which is ~1/10 the value of p(g3T2-O) but ~10 times that of p(g3T2-Se). The frequency dependent g_m of p(g3T2-Te) gave a $f_R/f_T = 6.5 \times 10^{-3}$, similar to that of p(g3T2-S), but much better than p(g3T2-Se) which shares a majority edge-on orientation. This would imply that moderately edge-on oriented 2-D crystallites are more detrimental to ionic transport in OECTs than the well oriented edge-on 3-D crystallites. While this rationale considers only the crystallite effects, disregarding the amorphous domains, crystallinity has previously been observed to greatly effect ion transport. 48,62 In summary, across the polymer series, as with electronic transport, microstructure seems key in determining ionic transport. But as is often the case for mixed conductors, microstructural control of ionic and electronic transport presents a balancing act (if not an outright

competition),⁶³ with the microstructure maximizing ionic transport also suppressing electronic transport and vice versa.

CONCLUSION

A series of oligoethylene glycol substituted bithiophene chalcogenophene alternating copolymers were synthesized and investigated for mixed conducting applications. Chalcogenophene heteroatom was found to have a profound effect on polymer microstructure, tuning 2-D π -stacked crystallites from face- to edge-on when the chalcogenophene heteroatom was varied from O to S to Se. In the case of the heaviest/largest chalcogenophene heteroatom investigated, Te, distinct well oriented 3-D crystallites were induced that had extensive ordering along the direction of the conjugated backbone (that was absent in the O, S, and Se polymers). The degree to which the heteroatom determined the microstructure was dependent on the side-chain length, with longer side-chains attenuating the heteroatom effects. In situ structural studies revealed that the heteroatom dependent difference in crystallite ordering persisted even in device relevant conditions when these polymer films were infiltrated with electrolyte and electrochemically doped.

Mixed conducting properties were found to be strongly correlated with thin film microstructure. The distinct well oriented 3-D ordering of p(g3T2-Te) produced OECTs with high figures of merit ($\mu_{hole} = 3.60 \text{ cm}^2\text{V}^{-1}\text{s}^{-1}$ and $\mu \times C^* = 483 \text{ Fcm}^{-1}\text{V}^{-1}\text{s}^{-1}$), low threshold voltage ($V_T = 0.04 \text{ V}$), and very sharp device turn on (S.S. = 44 mV/decade), reflecting efficient electronic charge transport and likely a narrow density and low trap density.^{64,65} Ionic transport was found to be dependent on the alignment of the ionophilic inter-lamellar spaces with respect to the direction of ionic transport.

Aside from producing well-ordered high performance OMIECs through heteroatom substitution, learning from these heteroatom effects provides rational structural targets for high performing OMIECs and OECTs. Beyond heteroatom substitution (which brings with it issues of material and device stability), these microstructures that benefit mixed conduction are likely achievable through alternate means, such as solution preaggregation,⁶⁶ film post-processing,⁴⁷ or film/fiber strain alignment.⁶⁷ Thus, this study both maps a new route for microstructural control of OMIECs, but also provides direction for future synthetic, structural, and processing studies.

ASSOCIATED CONTENT

Supporting Information. The Supporting Information is available free of charge at

Additional information and data relating to monomer and polymer synthesis and characterization, cyclic voltammetry, spectroelectrochemistry, ex situ X-ray characterization, in situ X-ray characterization, electrochemical impedance spectroscopy, OECT output curves, OECT subthreshold behavior, OECT degradation, and OECT frequency dependent behavior.

AUTHOR INFORMATION

Corresponding Authors

*Jonathan Rivnay. Department of Biomedical Engineering, Northwestern University,2145
Sheridan Rd, Evanston, IL 60208, USA. Department of Materials Science and Engineering,
Northwestern University, 2220 Campus Drive, Evanston, IL 60208, USA. Simpson Querrey
Institute, Northwestern University, Chicago, Illinois 60611, USA. Email:
jrivnay@northwestern.edu

*Iain McCulloch. Department of Chemistry, Chemistry Research Laboratory, University of Oxford, Oxford, OX1 3TA, UK. Email: iain.mcculloch@chem.ox.ac.uk

Present Addresses

†Materials and Manufacturing Directorate, Air Force Research Laboratory, Wright-Patterson Air Force Base, Ohio 45433, USA. UES, Inc., Dayton, Ohio 45432, USA.

Author Contributions

‡B.D. Paulsen, D. Meli, and M. Moser contributed equally.

Notes

The authors declare no competing financial interests.

ACKNOWLEDGMENTS

J.R. gratefully acknowledges funding support from Sloan under award no. FG-2019-12046. R.W., B.D.P., and J.R. acknowledge support from the National Science Foundation grant no. NSF DMR-1751308. R.W., D.M., and J.R. acknowledge funding from King Abdullah University of Science and Technology Office of Sponsored Research (OSR) under award no. OSR-2019-CRG8-4086. This work utilized the Keck-II facility of Northwestern University's NUANCE Center and Northwestern University Micro/Nano Fabrication Facility (NUFAB), which are both partially supported by the Soft and Hybrid Nanotechnology Experimental (SHyNE) Resource (NSF ECCS-1542205), the Materials Research Science and Engineering Center (NSF DMR-1720139), the State of Illinois, and Northwestern University. Additionally, the KeckII facility is partially supported by the International Institute for Nanotechnology (IIN); the Keck Foundation; and the State of Illinois, through the IIN. This research used resources of the Advanced Photon Source, a U.S. Department

of Energy (DOE) Office of Science User Facility operated for the DOE Office of Science by Argonne National Laboratory under Contract No. DE-AC02-06CH11357. In addition, use of the Stanford Synchrotron Radiation Lightsource, SLAC National Accelerator Laboratory, is supported by the U.S. Department of Energy, Office of Science, Office of Basic Energy Sciences under Contract No. DE-AC02-76SF00515. The authors gratefully acknowledge Christopher Takacs for beamline support at SSRL.

REFERENCES

- (1) Paulsen, B. D.; Tybrandt, K.; Stavrinidou, E.; Rivnay, J. Organic Mixed Ionic–Electronic Conductors. *Nat. Mater.* **2020**, *19* (1), 13–26. https://doi.org/10.1038/s41563-019-0435-z.
- (2) Uke, S. J.; Mardikar, S. P.; Kumar, A.; Kumar, Y.; Gupta, M.; Kumar, Y. A Review of π-Conjugated Polymer-Based Nanocomposites for Metal-Ion Batteries and Supercapacitors. *R. Soc. Open Sci.* **2021**, *8* (10), 210567. https://doi.org/10.1098/rsos.210567.
- (3) Melling, D.; Martinez, J. G.; Jager, E. W. H. Conjugated Polymer Actuators and Devices: Progress and Opportunities. *Adv. Mater.* **2019**, *31* (22), 1808210. https://doi.org/10.1002/adma.201808210.
- (4) Kim, J.; Rémond, M.; Kim, D.; Jang, H.; Kim, E. Electrochromic Conjugated Polymers for Multifunctional Smart Windows with Integrative Functionalities. *Adv. Mater. Technol.* **2020**, 5 (6), 1900890. https://doi.org/10.1002/admt.201900890.
- (5) Gao, J. Polymer Light-Emitting Electrochemical Cells—Recent Advances and Future Trends. *Curr. Opin. Electrochem.* **2018**, 7, 87–94. https://doi.org/10.1016/j.coelec.2017.10.027.
- (6) van de Burgt, Y.; Melianas, A.; Keene, S. T.; Malliaras, G.; Salleo, A. Organic Electronics for Neuromorphic Computing. *Nat. Electron.* **2018**, *1* (7), 386–397. https://doi.org/10.1038/s41928-018-0103-3.
- (7) Gumyusenge, A.; Melianas, A.; Keene, S. T.; Salleo, A. Materials Strategies for Organic Neuromorphic Devices. *Annu. Rev. Mater. Res.* **2021**, *51* (1), 47–71. https://doi.org/10.1146/annurev-matsci-080619-111402.
- (8) Ohayon, D.; Inal, S. Organic Bioelectronics: From Functional Materials to Next-Generation Devices and Power Sources. *Adv. Mater.* **2020**, *n/a* (n/a), 2001439. https://doi.org/10.1002/adma.202001439.
- (9) Vagin, M.; Gueskine, V.; Mitraka, E.; Wang, S.; Singh, A.; Zozoulenko, I.; Berggren, M.; Fabiano, S.; Crispin, X. Negatively-Doped Conducting Polymers for Oxygen Reduction Reaction. *Adv. Energy Mater.* **2021**, *11* (3), 2002664. https://doi.org/10.1002/aenm.202002664.
- (10) Mitraka, E.; Gryszel, M.; Vagin, M.; Jafari, M. J.; Singh, A.; Warczak, M.; Mitrakas, M.; Berggren, M.; Ederth, T.; Zozoulenko, I.; Crispin, X.; Głowacki, E. D. Electrocatalytic

- Production of Hydrogen Peroxide with Poly(3,4-Ethylenedioxythiophene) Electrodes. *Adv. Sustain. Syst.* **2019**, *3* (2), 1800110. https://doi.org/10.1002/adsu.201800110.
- (11) He, Y.; Kukhta, N. A.; Marks, A.; Luscombe, C. K. The Effect of Side Chain Engineering on Conjugated Polymers in Organic Electrochemical Transistors for Bioelectronic Applications. *J. Mater. Chem. C* **2022**, *10* (7), 2314–2332. https://doi.org/10.1039/D1TC05229B.
- (12) Moser, M.; Savagian, L. R.; Savva, A.; Matta, M.; Ponder, J. F.; Hidalgo, T. C.; Ohayon, D.; Hallani, R.; Reisjalali, M.; Troisi, A.; Wadsworth, A.; Reynolds, J. R.; Inal, S.; McCulloch, I. Ethylene Glycol-Based Side Chain Length Engineering in Polythiophenes and Its Impact on Organic Electrochemical Transistor Performance. *Chem. Mater.* **2020**, *32* (15), 6618–6628. https://doi.org/10.1021/acs.chemmater.0c02041.
- (13) Moser, M.; Hidalgo, T. C.; Surgailis, J.; Gladisch, J.; Ghosh, S.; Sheelamanthula, R.; Thiburce, Q.; Giovannitti, A.; Salleo, A.; Gasparini, N.; Wadsworth, A.; Zozoulenko, I.; Berggren, M.; Stavrinidou, E.; Inal, S.; McCulloch, I. Side Chain Redistribution as a Strategy to Boost Organic Electrochemical Transistor Performance and Stability. *Adv. Mater.* **2020**, *32* (37), 2002748. https://doi.org/10.1002/adma.202002748.
- (14) Moser, M.; Savva, A.; Thorley, K.; Paulsen, B. D.; Hidalgo, T. C.; Ohayon, D.; Chen, H.; Giovannitti, A.; Marks, A.; Gasparini, N.; Wadsworth, A.; Rivnay, J.; Inal, S.; McCulloch, I. Polaron Delocalization in Donor–Acceptor Polymers and Its Impact on Organic Electrochemical Transistor Performance. *Angew. Chem. Int. Ed.* **2021**, *60* (14), 7777–7785. https://doi.org/10.1002/anie.202014078.
- (15) Advincula, A. A.; Jones, A. L.; Thorley, K. J.; Österholm, A. M.; Ponder, J. F.; Reynolds, J. R. Probing Comonomer Selection Effects on Dioxythiophene-Based Aqueous-Compatible Polymers for Redox Applications. *Chem. Mater.* **2022**, *34* (10), 4633–4645. https://doi.org/10.1021/acs.chemmater.2c00511.
- (16) Parr, Z. S.; Borges-González, J.; Rashid, R. B.; Thorley, K. J.; Meli, D.; Paulsen, B. D.; Strzalka, J.; Rivnay, J.; Nielsen, C. B. From P- to n-Type Mixed Conduction in Isoindigo-Based Polymers through Molecular Design. *Adv. Mater.* **2022**, *34* (14), 2107829. https://doi.org/10.1002/adma.202107829.
- (17) Parr, Z. S.; Halaksa, R.; Finn, P. A.; Rashid, R. B.; Kovalenko, A.; Weiter, M.; Rivnay, J.; Krajčovič, J.; Nielsen, C. B. Glycolated Thiophene-Tetrafluorophenylene Copolymers for Bioelectronic Applications: Synthesis by Direct Heteroarylation Polymerisation. *ChemPlusChem* **2019**, *84* (9), 1384–1390. https://doi.org/10.1002/cplu.201900254.
- (18) Yang, W.; Feng, K.; Ma, S.; Liu, B.; Wang, Y.; Ding, R.; Jeong, S. Y.; Woo, H. Y.; Chan, P. K. L.; Guo, X. High-Performance n-Type Polymeric Mixed Ionic-Electronic Conductors: The Impacts of Halogen Functionalization. *Adv. Mater.* **2023**, 2305416. https://doi.org/10.1002/adma.202305416.
- (19) Feng, K.; Shan, W.; Wang, J.; Lee, J.; Yang, W.; Wu, W.; Wang, Y.; Kim, B. J.; Guo, X.; Guo, H. Cyano-Functionalized n-Type Polymer with High Electron Mobility for High-Performance Organic Electrochemical Transistors. *Adv. Mater.* **2022**, *34* (24), 2201340. https://doi.org/10.1002/adma.202201340.
- (20) Chen, X.; Marks, A.; Paulsen, B. D.; Wu, R.; Rashid, R. B.; Chen, H.; Alsufyani, M.; Rivnay, J.; McCulloch, I. *N*-Type Rigid Semiconducting Polymers Bearing Oligo(Ethylene Glycol) Side Chains for High-Performance Organic Electrochemical Transistors. *Angew. Chem. Int. Ed.* **2021**, *60* (17), 9368–9373. https://doi.org/10.1002/anie.202013998.

- (21) Sachinthani, K. A. N.; Panchuk, J. R.; Wang, Y.; Zhu, T.; Sargent, E. H.; Seferos, D. S. Thiophene- and Selenophene-Based Conjugated Polymeric Mixed Ionic/Electronic Conductors. *J. Chem. Phys.* **2021**, *155* (13), 134704. https://doi.org/10.1063/5.0064858.
- (22) Kim, J.; Ren, X.; Zhang, Y.; Fazzi, D.; Manikandan, S.; Andreasen, J. W.; Sun, X.; Ursel, S.; Un, H.; Peralta, S.; Xiao, M.; Town, J.; Marathianos, A.; Roesner, S.; Bui, T.; Ludwigs, S.; Sirringhaus, H.; Wang, S. Efficient N-Type Organic Electrochemical Transistors and Field-Effect Transistors Based on PNDI-Copolymers Bearing Fluorinated Selenophene-Vinylene-Selenophenes. *Adv. Sci.* **2023**, 2303837. https://doi.org/10.1002/advs.202303837.
- (23) Ponder, J. F.; Pittelli, S. L.; Reynolds, J. R. Heteroatom Role in Polymeric Dioxyselenophene/Dioxythiophene Systems for Color and Redox Control. *ACS Macro Lett.* **2016**, *5* (6), 714–717. https://doi.org/10.1021/acsmacrolett.6b00250.
- (24) Schafer, E. A.; Wu, R.; Meli, D.; Tropp, J.; Moser, M.; McCulloch, I.; Paulsen, B. D.; Rivnay, J. Sources and Mechanism of Degradation in P-Type Thiophene-Based Organic Electrochemical Transistors. *ACS Appl. Electron. Mater.* **2022**, *4* (4), 1391–1404. https://doi.org/10.1021/acsaelm.1c01171.
- (25) Carrera, E. I.; Seferos, D. S. Semiconducting Polymers Containing Tellurium: Perspectives Toward Obtaining High-Performance Materials. *Macromolecules* **2015**, *48* (2), 297–308. https://doi.org/10.1021/ma502307b.
- (26) Ye, S.; Lotocki, V.; Xu, H.; Seferos, D. S. Group 16 Conjugated Polymers Based on Furan, Thiophene, Selenophene, and Tellurophene. *Chem. Soc. Rev.* **2022**, *51* (15), 6442–6474. https://doi.org/10.1039/D2CS00139J.
- (27) Hollinger, J.; Gao, D.; Seferos, D. S. Selenophene Electronics. *Isr. J. Chem.* **2014**, *54* (5–6), 440–453. https://doi.org/10.1002/ijch.201400011.
- (28) Nielsen, C. B.; Giovannitti, A.; Sbircea, D.-T.; Bandiello, E.; Niazi, M. R.; Hanifi, D. A.; Sessolo, M.; Amassian, A.; Malliaras, G. G.; Rivnay, J.; McCulloch, I. Molecular Design of Semiconducting Polymers for High-Performance Organic Electrochemical Transistors. *J. Am. Chem. Soc.* **2016**, *138* (32), 10252–10259. https://doi.org/10.1021/jacs.6b05280.
- (29) Dai, Y.; Dai, S.; Li, N.; Li, Y.; Moser, M.; Strzalka, J.; Prominski, A.; Liu, Y.; Zhang, Q.; Li, S.; Hu, H.; Liu, W.; Chatterji, S.; Cheng, P.; Tian, B.; McCulloch, I.; Xu, J.; Wang, S. Stretchable Redox-Active Semiconducting Polymers for High-Performance Organic Electrochemical Transistors. *Adv. Mater.* **2022**, *34* (23), 2201178. https://doi.org/10.1002/adma.202201178.
- (30) Parr, Z. S.; Rashid, R. B.; Paulsen, B. D.; Poggi, B.; Tan, E.; Freeley, M.; Palma, M.; Abrahams, I.; Rivnay, J.; Nielsen, C. B. Semiconducting Small Molecules as Active Materials for P-Type Accumulation Mode Organic Electrochemical Transistors. *Adv. Electron. Mater.* **2020**, *6* (6), 2000215. https://doi.org/10.1002/aelm.202000215.
- (31) Jiang, Z. *GIXSGUI*: A MATLAB Toolbox for Grazing-Incidence X-Ray Scattering Data Visualization and Reduction, and Indexing of Buried Three-Dimensional Periodic Nanostructured Films. *J. Appl. Crystallogr.* **2015**, *48* (3), 917–926. https://doi.org/10.1107/S1600576715004434.
- (32) Paulsen, B. D.; Giovannitti, A.; Wu, R.; Strzalka, J.; Zhang, Q.; Rivnay, J.; Takacs, C. J. Electrochemistry of Thin Films with In Situ/Operando Grazing Incidence X-Ray Scattering: Bypassing Electrolyte Scattering for High Fidelity Time Resolved Studies. *Small* **2021**, *17* (42), 2103213. https://doi.org/10.1002/smll.202103213.

- (33) Seitz, D. E.; Lee, S.-H.; Hanson, R. N.; Bottaro, J. C. Synthesis and Reactivity of the 2,5-Bis(Trimethylstannyl) Derivatives of Thiophene and Furan. *Synth. Commun.* **1983**, *13* (2), 121–128. https://doi.org/10.1080/00397918308061969.
- (34) Jahnke, A. A.; Howe, G. W.; Seferos, D. S. Polytellurophenes with Properties Controlled by Tellurium-Coordination. *Angew. Chem. Int. Ed.* **2010**, *49* (52), 10140–10144. https://doi.org/10.1002/anie.201005664.
- (35) Sweat, D. P.; Stephens, C. E. A Modified Synthesis of Tellurophene Using NaBH4 to Generate Sodium Telluride. *J. Organomet. Chem.* **2008**, *693* (14), 2463–2464. https://doi.org/10.1016/j.jorganchem.2008.04.022.
- (36) Planells, M.; Schroeder, B. C.; McCulloch, I. Effect of Chalcogen Atom Substitution on the Optoelectronic Properties in Cyclopentadithiophene Polymers. *Macromolecules* **2014**, *47* (17), 5889–5894. https://doi.org/10.1021/ma5014308.
- (37) Ashraf, R. S.; Meager, I.; Nikolka, M.; Kirkus, M.; Planells, M.; Schroeder, B. C.; Holliday, S.; Hurhangee, M.; Nielsen, C. B.; Sirringhaus, H.; McCulloch, I. Chalcogenophene Comonomer Comparison in Small Band Gap Diketopyrrolopyrrole-Based Conjugated Polymers for High-Performing Field-Effect Transistors and Organic Solar Cells. *J. Am. Chem. Soc.* **2015**, *137* (3), 1314–1321. https://doi.org/10.1021/ja511984q.
- (38) Zozoulenko, I.; Singh, A.; Singh, S. K.; Gueskine, V.; Crispin, X.; Berggren, M. Polarons, Bipolarons, And Absorption Spectroscopy of PEDOT. *ACS Appl. Polym. Mater.* **2019**, *1* (1), 83–94. https://doi.org/10.1021/acsapm.8b00061.
- (39) Sahalianov, I.; Hynynen, J.; Barlow, S.; Marder, S. R.; Müller, C.; Zozoulenko, I. UV-to-IR Absorption of Molecularly p-Doped Polythiophenes with Alkyl and Oligoether Side Chains: Experiment and Interpretation Based on Density Functional Theory. *J. Phys. Chem. B* **2020**, *124* (49), 11280–11293. https://doi.org/10.1021/acs.jpcb.0c08757.
- (40) Rivnay, J.; Mannsfeld, S. C. B.; Miller, C. E.; Salleo, A.; Toney, M. F. Quantitative Determination of Organic Semiconductor Microstructure from the Molecular to Device Scale. *Chem. Rev.* **2012**, *112* (10), 5488–5519. https://doi.org/10.1021/cr3001109.
- (41) Lee, H. W.; Kim, H. S.; Kim, D.; Yoon, M.; Lee, J.; Hwang, D.-H. Comparative Study of Charge-Transport Behavior of Edge-on- and Face-on-Oriented Diketopyrrolopyrrole-Based Conjugated Copolymers Bearing Chalcogenophene Units. *Chem. Mater.* **2022**, *34* (1), 314–324. https://doi.org/10.1021/acs.chemmater.1c03626.
- (42) Huang, C.-L.; Pao, Y.-C.; Chen, S.-Y.; Hsu, J.-Y.; Tsai, C.-L.; Cheng, Y.-J. Synthesis of Asymmetric Benzotrithiophene/Benzotriselenophene Building Blocks and Their Donor Acceptor Copolymers: Chalcogen Effect on Face-on/Edge-on Orientations and Charge Transport. *Macromolecules* 2023, 56 (17), 6722–6732. https://doi.org/10.1021/acs.macromol.3c01062.
- (43) Brinkmann, M.; Gonthier, E.; Bogen, S.; Tremel, K.; Ludwigs, S.; Hufnagel, M.; Sommer, M. Segregated versus Mixed Interchain Stacking in Highly Oriented Films of Naphthalene Diimide Bithiophene Copolymers. *ACS Nano* **2012**, *6* (11), 10319–10326. https://doi.org/10.1021/nn304213h.
- (44) Trefz, D.; Gross, Y. M.; Dingler, C.; Tkachov, R.; Hamidi-Sakr, A.; Kiriy, A.; McNeill, C. R.; Brinkmann, M.; Ludwigs, S. Tuning Orientational Order of Highly Aggregating P(NDI2OD-T2) by Solvent Vapor Annealing and Blade Coating. *Macromolecules* **2019**, *52* (1), 43–54. https://doi.org/10.1021/acs.macromol.8b02176.
- (45) Zhong, Y.; Biniek, L.; Leclerc, N.; Ferry, S.; Brinkmann, M. Segregated versus Disordered Stacking in Two Low Bandgap Alternated Copolymers for Photovoltaic Applications: Impact

- of Polymorphism on Optical Properties. *Macromolecules* **2018**, *51* (11), 4238–4249. https://doi.org/10.1021/acs.macromol.8b00378.
- (46) Peng, Z.; Ye, L.; Ade, H. Understanding, Quantifying, and Controlling the Molecular Ordering of Semiconducting Polymers: From Novices to Experts and Amorphous to Perfect Crystals. *Mater. Horiz.* **2022**, *9* (2), 577–606. https://doi.org/10.1039/D0MH00837K.
- (47) Kim, S.-M.; Kim, C.-H.; Kim, Y.; Kim, N.; Lee, W.-J.; Lee, E.-H.; Kim, D.; Park, S.; Lee, K.; Rivnay, J.; Yoon, M.-H. Influence of PEDOT:PSS Crystallinity and Composition on Electrochemical Transistor Performance and Long-Term Stability. *Nat. Commun.* **2018**, *9* (1), 3858. https://doi.org/10.1038/s41467-018-06084-6.
- (48) Kim, J. H.; Ahmad, Z.; Kim, Y.; Kim, W.; Ahn, H.; Lee, J.-S.; Yoon, M.-H. Decoupling Critical Parameters in Large-Range Crystallinity-Controlled Polypyrrole-Based High-Performance Organic Electrochemical Transistors. *Chem. Mater.* **2020**, *32* (19), 8606–8618. https://doi.org/10.1021/acs.chemmater.0c02936.
- (49) Tropp, J.; Meli, D.; Rivnay, J. Organic Mixed Conductors for Electrochemical Transistors. *Matter* **2023**, S2590238523002199. https://doi.org/10.1016/j.matt.2023.05.001.
- (50) Ye, S.; Janasz, L.; Zajaczkowski, W.; Manion, J. G.; Mondal, A.; Marszalek, T.; Andrienko, D.; Müllen, K.; Pisula, W.; Seferos, D. S. Self-Organization and Charge Transport Properties of Selenium and Tellurium Analogues of Polythiophene. *Macromol. Rapid Commun.* **2019**, *40* (1), 1800596. https://doi.org/10.1002/marc.201800596.
- (51) Rivnay, J.; Noriega, R.; Northrup, J. E.; Kline, R. J.; Toney, M. F.; Salleo, A. Structural Origin of Gap States in Semicrystalline Polymers and the Implications for Charge Transport. *Phys. Rev. B* **2011**, *83* (12), 121306. https://doi.org/10.1103/PhysRevB.83.121306.
- (52) Noriega, R.; Rivnay, J.; Vandewal, K.; Koch, F. P. V.; Stingelin, N.; Smith, P.; Toney, M. F.; Salleo, A. A General Relationship between Disorder, Aggregation and Charge Transport in Conjugated Polymers. *Nat. Mater.* **2013**, *12* (11), 1038–1044. https://doi.org/10.1038/nmat3722.
- (53) Hynynen, J.; Kiefer, D.; Müller, C. Influence of Crystallinity on the Thermoelectric Power Factor of P3HT Vapour-Doped with F4TCNQ. *RSC Adv.* **2018**, *8* (3), 1593–1599. https://doi.org/10.1039/C7RA11912G.
- (54) Paulsen, B. D.; Frisbie, C. D. Dependence of Conductivity on Charge Density and Electrochemical Potential in Polymer Semiconductors Gated with Ionic Liquids. *J. Phys. Chem. C* **2012**, *116* (4), 3132–3141. https://doi.org/10.1021/jp2093934.
- (55) Kunugi, Y.; Harima, Y.; Yamashita, K.; Ohta, N.; Ito, S. Charge Transport in a Regioregular Poly(3-Octylthiophene)Film. *J. Mater. Chem.* **2000**, *10* (12), 2673–2677. https://doi.org/10.1039/B004434M.
- (56) Harima, Y.; Kunugi, Y.; Yamashita, K.; Shiotani, M. Determination of Mobilities of Charge Carriers in Electrochemically Anion-Doped Polythiophene Film. *Chem. Phys. Lett.* **2000**, *317* (3), 310–314. https://doi.org/10.1016/S0009-2614(99)01378-0.
- (57) Harima, Y.; Eguchi, T.; Yamashita, K. Enhancement of Carrier Mobilities in Poly(3-Methylthiophene) by an Electrochemical Doping. *Synth. Met.* **1998**, *95* (1), 69–74. https://doi.org/10.1016/S0379-6779(98)00035-6.
- (58) Wang, S.; Ha, M.; Manno, M.; Daniel Frisbie, C.; Leighton, C. Hopping Transport and the Hall Effect near the Insulator–Metal Transition in Electrochemically Gated Poly(3-Hexylthiophene) Transistors. *Nat. Commun.* **2012**, *3* (1), 1210. https://doi.org/10.1038/ncomms2213.

- (59) Tarabella, G.; Santato, C.; Yang, S. Y.; Iannotta, S.; Malliaras, G. G.; Cicoira, F. Effect of the Gate Electrode on the Response of Organic Electrochemical Transistors. *Appl. Phys. Lett.* **2010**, *97* (12), 123304. https://doi.org/10.1063/1.3491216.
- (60) Marsh, A. V.; Heeney, M. Conjugated Polymers Based on Selenophene Building Blocks. *Polym. J.* **2023**, *55* (4), 375–385. https://doi.org/10.1038/s41428-022-00731-y.
- (61) Zhang, S.; Ding, P.; Ruoko, T.; Wu, R.; Stoeckel, M.; Massetti, M.; Liu, T.; Vagin, M.; Meli, D.; Kroon, R.; Rivnay, J.; Fabiano, S. Toward Stable p-Type Thiophene-Based Organic Electrochemical Transistors. *Adv. Funct. Mater.* **2023**, 2302249. https://doi.org/10.1002/adfm.202302249.
- (62) Flagg, L. Q.; Bischak, C. G.; Onorato, J. W.; Rashid, R. B.; Luscombe, C. K.; Ginger, D. S. Polymer Crystallinity Controls Water Uptake in Glycol Side-Chain Polymer Organic Electrochemical Transistors. *J. Am. Chem. Soc.* **2019**, *141* (10), 4345–4354. https://doi.org/10.1021/jacs.8b12640.
- (63) Paulsen, B. D.; Fabiano, S.; Rivnay, J. Mixed Ionic-Electronic Transport in Polymers. *Annu. Rev. Mater. Res.* **2021**, *51* (1), 73–99. https://doi.org/10.1146/annurev-matsci-080619-101319.
- (64) Kalb, W. L.; Batlogg, B. Calculating the Trap Density of States in Organic Field-Effect Transistors from Experiment: A Comparison of Different Methods. *Phys. Rev. B* **2010**, *81* (3), 035327. https://doi.org/10.1103/PhysRevB.81.035327.
- (65) Nakano, K.; Kaji, Y.; Tajima, K. Impact of Narrowing Density of States in Semiconducting Polymers on Performance of Organic Field-Effect Transistors. *Small* **2023**, *19* (3), 2205570. https://doi.org/10.1002/smll.202205570.
- (66) Eller, F.; Wenzel, F. A.; Hildner, R.; Havenith, R. W. A.; Herzig, E. M. Spark Discharge Doping—Achieving Unprecedented Control over Aggregate Fraction and Backbone Ordering in Poly(3-hexylthiophene) Solutions. *Small* **2023**, *19* (21), 2207537. https://doi.org/10.1002/smll.202207537.
- (67) Kim, Y.; Noh, H.; Paulsen, B. D.; Kim, J.; Jo, I.; Ahn, H.; Rivnay, J.; Yoon, M. Strain-Engineering Induced Anisotropic Crystallite Orientation and Maximized Carrier Mobility for High-Performance Microfiber-Based Organic Bioelectronic Devices. *Adv. Mater.* **2021**, *33* (10), 2007550. https://doi.org/10.1002/adma.202007550.

ToC Graphic

